An Improved Direct Forcing Immersed Boundary Method With Integrated Mooring Algorithm for Floating Offshore Wind Turbines

Ahmet Soydan[a,1,*], Widar. W. Wang[a], Hans Bihs[a]

[a]*Norwegian University of Science and Technology*
Høgskoleringen 7A, 7491 Trondheim, Norway

Abstract

An upgraded direct forcing immersed boundary method is implemented in the open-source hydrodynamic framework REEF3D::CFD for simulating the six-degrees-of-freedom (6DOF) motions of a floating offshore wind turbine (FOWT) based on the OC5 semi-submersible design. The direct forcing method is enhanced with a new density interpolation method across the fluid-structure interface that removes unphysical spurious phenomena and ensures stable and accurate wave load calculations on floating objects. A quasi-static algorithm is used for modeling the mooring system of the OC5 platform and restraining its motions in waves. The Navier-Stokes equations are solved on a staggered structured rectilinear grid for the hydrodynamic simulations. The level-set method is used to capture the free surface of the ocean waves. A ray-casting algorithm is employed to get inside-outside information near the fluid-solid interface while maintaining the underlying Cartesian grid in the hydrodynamic domain. The performance and accuracy of the mooring algorithm are compared to the widely-used mooring model MoorDyn, which is coupled to the hydrodynamic solver in REEF3D::CFD. The study demonstrates that the enhanced direct forcing method with the integrated quasi-static mooring algorithm in REEF3D::CFD provides a robust and accurate tool, suitable for the numerical analysis of the state-of-the-art FOWT in ocean waves.

Keywords: 6DOF, floating, level set method, immersed boundary

1. Introduction

Floating offshore wind turbines (FOWTs) are a quite complicated system involving various aspects of physics. The complex structure of FOWT operates in harsh environmental conditions, incorporating aerodynamics, hydrodynamics, and structural dynamics effects. Additionally, mooring dynamics play a key role in these coupled multi-physics problems, making numerical simulations extremely challenging. High-fidelity Computational Fluid

*I am corresponding author

Email addresses: ahmet.soydan@ntnu.no (Ahmet Soydan), widar.w.wang@ntnu.no (Widar. W. Wang), hans.bihs@ntnu.no (Hans Bihs)

Dynamics (CFD) tools are frequently used to predict floating-body motions, the nonlinearity of the flow as well as multi-physics coupling.

Several numerical verification and validation (V&V) studies have been conducted by researchers for the DeepCwind semi-submersible platform to assess the reliability of CFD tools. Burmester et al. [1] investigated surge decay simulation of the FOWT with a catenary mooring line system for validation purposes using open-source CFD code ReFRESCO [2]. Wang et al. [3], on the other hand, carried out a V&V study in pitch free-decay motion with both linear and dynamic mooring models, revealing significant improvements with the dynamic mooring model. Furthermore, Wang et al. [4] performed a comprehensive V&V study under regular waves, coupling the dynamic mooring model MOORING3D [5] with ReFRESCO to simulate mooring dynamics. As a further iteration of this field, aerodynamic loads on the FOWT system were also included in numerical simulations. Cheng et al. [6] presented a fully coupled aero-hydrodynamic numerical model based on the open-source CFD tool OpenFOAM. The unsteady actuator line model (UALM) [7] was used for aerodynamic analysis of wind turbine and mooring dynamics was modeled with three catenary lines. Additionally, Liu et al. [8] employed a fully coupled CFD simulation in terms of aerodynamics, hydrodynamics, and mooring dynamics for the FOWT using OpenFOAM under various wave conditions. A quasi-static mooring model was coupled with the solver and overset mesh method was applied for the rigid-body motion. The reciprocal interaction between the wind turbine and the floating platform was analyzed according to the wind speeds and wave conditions. The commercial CFD code STAR-CCM + is also widely used for fully coupled FOWT simulations. Tran and Kim [9], [10] conducted a full-scale multi-physical FOWT analysis based on an overset mesh technique for the free-decay test and regular wave conditions. The mooring dynamics were modeled with a quasi-static mooring model, and numerical results were validated with experimental data.

In this study, an upgraded direct forcing immersed boundary method is implemented in the open-source hydrodynamic framework REEF3D [11] for simulating a semi-submersible FOWT OC5 with a full scale. The numerical model specifically focuses on addressing fluid-structure interactions [12, 13], as well as the analysis of floating structure restrained by mooring lines [14, 15]. The direct forcing method is enhanced with a new density interpolation method across the fluid-structure interface that removes unphysical spurious velocity of the fluid-structure interface and ensures stable and accurate wave load calculations on floating objects. A quasi-static mooring model is available within this framework[14]. The widely-used lumped-mass mooring model MoorDyn [16] is also coupled to the hydrodynamic solver in REEF3D::CFD to assess the reliability of the different methods. The numerical method is tested and validated with experimental data considering the motion responses of the FOWT under two different regular wave conditions.

2. NUMERICAL MODEL

The numerical framework REEF3D::CFD [11] solves the three-dimensional incompressible Reynolds-Averaged Navier–Stokes equations (RANS). The numerical model is based on a staggered rectilinear grid along with high-order spatial and temporal discretization

schemes. The model includes a rigid-body fluid-structure interaction (FSI) algorithm to solve floating body and wave interaction and a quasi-static mooring dynamics model [14] for the mooring dynamics. Details are given in the following sections.

2.1. REEF3D::CFD

The three-dimensional Navier-Stokes equations and the continuity equation, which describe the conservation of mass and momentum for incompressible flow, are written as:

$$\nabla \cdot \mathbf{u} = 0 \tag{1}$$

$$\frac{\partial \mathbf{u}}{\partial t} + \mathbf{u} \cdot \nabla \mathbf{u} = -\frac{1}{\rho}\nabla p + \frac{1}{\rho}\nabla \cdot \left(\mu \left[\nabla \mathbf{u} + \nabla \mathbf{u}^T\right]\right) + \mathbf{g} \tag{2}$$

where $\mathbf{u}$ is the velocity vector, ρ is the density of the fluid, p is the pressure, μ is the dynamic viscosity, and $\mathbf{g}$ is the acceleration vector due to gravity [11, 17].

The implicit representation of the transition between the air and water phases is defined by the zero level set of the smooth signed distance function ϕ [18].

$$\phi(\vec{x}, t) = \begin{cases} > 0 & \text{if } \vec{x} \in \text{phase 1} \\ = 0 & \text{if } \vec{x} \in \Gamma \\ < 0 & \text{if } \vec{x} \in \text{phase 2} \end{cases} \tag{3}$$

A convection equation is solved for the propagation of the level set function.

$$\frac{\partial \phi}{\partial t} + \mathbf{u} \cdot \nabla \phi = 0 \tag{4}$$

After each time step, a PDE-based reinitializion equation [19] is solved to keep the signed distance properties. [19]:

$$\frac{\partial \phi}{\partial t} + \text{sign}(\phi)\left(|\nabla \phi| - 1\right) = 0 \tag{5}$$

Here, sign(ϕ) is the smoothed sign function [20]. To ensure the conservation of mass, the Eikonal equation $|\nabla \Phi| = 1$ should also be fulfilled.

The density and viscosity are calculated as:

$$\rho = \rho_w H(\phi) + \rho_a (1 - H(\phi)) \tag{6}$$

$$\nu = \nu_w H(\phi) + \nu_a (1 - H(\phi)) \tag{7}$$

where w and a stand for water and air properties, respectively. The smoothed Heaviside step function $H(\phi)$ is defined as:

$$H(\phi) = \begin{cases} = 0 & \text{if } \phi < -\epsilon \\ = \frac{1}{2}\left(1 + \frac{\phi}{\epsilon} + \frac{1}{\pi}\sin\left(\frac{\pi\phi}{\epsilon}\right)\right) & \text{if } |\phi| \leq \epsilon \\ = 1 & \text{if } \phi > \epsilon \end{cases} \tag{8}$$

where the thickness of the interface is $\epsilon = 2.1\Delta x$.

The finite differences method on a rectilinear staggered grid is used to solve the system of equations. For the convection terms, a fifth-order accurate weighted essentially non-oscillatory (WENO) scheme is employed, as described in [21]. The convection term in Eq. (4) is discretized with the fifth-order accurate Hamilton-Jacobi WENO method of [22]. The diffusion terms are handled using the second-order accurate central finite difference scheme. The pressure term in the RANS equation is solved using an incremental pressure-correction algorithm [23], following the approach outlined in [24]. The time derivatives, including those in Eq. (4) and Eq. (5) are solved by using the third-order accurate Total Variation Diminishing (TVD) Runge-Kutta scheme [25]. The numerical stability is kept with the time step size controlled by the CFL condition. The pressure correction is computed by solving the Poisson equation using the fully parallelized BiCGStab algorithm of the HYPRE library [26] with the geometric multigrid pre-conditioner [27] to enhance the computational efficiency [17].

2.2. Rigid-Body FSI Algorithm

A direct forcing immersed boundary approach is implemented in REEF3D::CFD to take into account the rigid body in the fluid domain. A forcing term $\mathbf{f}$ is added in the momentum equation to represent the solid velocity field following the derivation in [28].

$$\nabla \cdot \mathbf{u} = 0 \tag{9}$$

$$\frac{\partial \mathbf{u}}{\partial t} + \mathbf{u} \cdot \nabla \mathbf{u} = -\frac{1}{\rho}\nabla p + \mathbf{g} + \mathbf{f} \tag{10}$$

The forcing term is calculated as:

$$\mathbf{f}^{(n+1)} \approx \mathbf{f}^{(*)} = H\left(\Phi_s^{(*)}\right) \cdot \left(\frac{\mathbf{P}(\mathbf{u}^{(*)}) - \mathbf{u}^*}{\alpha_k \Delta t}\right) \tag{11}$$

Here, the smoothed Heaviside function $H(\Phi_s)$ is introduced to represent the transition from fluid to solid. The level set method [18] is used to identify the interface and added in the smoothed Heaviside function. A ray-casting algorithm [29] is used to determine the closest distance information of neighboring fluid cells to the solid boundary. The closest distance is transformed into a signed distance function Φ_s representing the floating body in the Eulerian domain. The signed distance function Φ_s is reinitialized with the PDE-based Eq. (5) [19]. $\mathbf{P(u)}$ and $\mathbf{u}^*$ represent the rigid body velocity and fluid velocity in each Runge-Kutta sub-step, respectively. α_k is a Runge-Kutta coefficient and Δt is time-step. The solid and fluid phases are separated by extending Eq. (6) and eq. (7) where s stands for the solid, and $H(\Phi_s)$ is the solid Heaviside function for the transition of the fluid to the solid.

$$\rho(\phi, \Phi_s) = \rho_s H(\Phi_s) + (1 - H(\Phi_s)) \cdot (\rho_w H(\phi) + \rho_a (1 - H(\phi))) \tag{12}$$

$$\nu(\phi, \Phi_s) = (1 - H(\Phi_s)) \cdot (\nu_w H(\phi) + \nu_a (1 - H(\phi))) \tag{13}$$

In this approach, the material properties of the solid body are assigned using Eqs. (12) and (13). However, this approach results in a high-density gradient in close proximity of the body which entails the use of finely refined cells around the solid body. Therefore, the transition layer between the fluid and the solid body needs to be relatively large to maintain stability. To address this issue, the fluid density and viscosity are set to be the same inside and outside the immersed boundary. Hence, the continuous fluid density treatment is implemented based on Eq. (6) and Eq. (7). This treatment removes artificial density gradients in the vicinity of the floating body and allows to use of a relatively coarser grid in the vicinity of the body and a thinner transition layer distinguishing the fluid and the solid body. The new density interpolation method removes unphysical spurious velocity and ensures stable and accurate wave load calculations on floating objects [17].

The intermediate solid body velocity field is defined as:

$$\mathbf{P}\left(\mathbf{u}^{(*)}\right) = \dot{x}_i + \omega_i \times r \tag{14}$$

Here, $\dot{x}_i$ is the translational rigid-body velocity vector, ω is the angular rigid body-velocity vector and r is the distance vector to the rigid body's center of gravity. An STL file geometry consisting of multiple non-connected triangles is used to represent the rigid body in the fluid domain. The fluid properties (pressure p, the viscous stress tensor τ) are integrated over the discrete solid surface Ω to calculate the body forces and momenta as below:

$$F_i = \int_{\Omega} (-\mathbf{n}p + \rho\nu\mathbf{n}\tau) d\Omega(\mathbf{x}) = \sum_{i=1}^{N} (-\mathbf{n}p + \rho\nu\mathbf{n}\tau)_i \cdot \Delta\Omega_i \tag{15}$$

$$M_i = \int_{\Omega} \mathbf{r} \times (-\mathbf{n}p + \rho\nu\mathbf{n}\tau) d\Omega(\mathbf{x}) = \sum_{i=1}^{N} \mathbf{r}_i \times (-\mathbf{n}p + \rho\nu\mathbf{n}\tau)_i \cdot \Delta\Omega_i \tag{16}$$

In this context, $\mathbf{n}$ represents the outward-pointing surface normal vector, while $\mathbf{r}$ denotes the distance vector to the center of gravity of the solid body. The contributions to pressure p and the viscous stress tensor τ from the discrete solid surface are summed to determine the global forces. The mooring forces are calculated as an external force and subsequently added to the total force during each runge-kutta substep.

2.3. Quasi-static mooring dynamics model

The finite element-based quasi-static mooring model was implemented in the numerical framework REEF3D as presented in [14]. The mooring line dynamics, neglecting bending stiffness, are explained [30] as:

$$\gamma \frac{\partial^2 \vec{r}}{\partial t^2} = \frac{\partial F_T \vec{f}}{\partial s} + \vec{F}_e \tag{17}$$

Here, $\vec{r}$ is the global coordinate position vector of the cable, γ represents the cable mass per unit length, F_T is the tension force magnitude, $\vec{f}$ is the unit vector in the same direction of the tension force, and $\vec{F}_e$ denotes the external forces, which include hydrodynamic and

gravitation effects. Eq. (17) is simplified, assuming that the flow is steady-state and the line motion is small in time:

$$\frac{\partial F_T \vec{f}}{\partial s} = -\vec{F}_e \tag{18}$$

The mooring line is discretized with N bars. The bars have the same length of l_t in two consecutive nodes P. The first node $P^{(0)}$ is connected to the bottom (anchor node) and the last node $P^{(N)}$ is connected to the floating body (fairlead node). The gravity force $\vec{F}_G^j$ contribution is applied at each node $P^{(j)}$. Hydrodynamic forces are calculated as drag forces using Morison's formula at each bar. The added mass forces are neglected. This formula contributes to the hydrodynamic mooring damping. The force equilibrium at each inner node can be found by separating the internal and external forces. The linear system of equations is yielded, which is solved iteratively by Gaussian elimination method.

$$\begin{pmatrix} \mathbf{T} \\ \mathbf{L} \end{pmatrix} \cdot \mathbf{F} = \begin{pmatrix} -(\mathbf{H}+\mathbf{G}) \\ \vec{x}\left(P^N\right) - \vec{x}\left(P^0\right) \end{pmatrix} \tag{19}$$

Here, $\mathbf{T}$ is a sub-matrix of tension forces, $\mathbf{L}$ is the bar lengths vector, $\mathbf{H}$ and $\mathbf{G}$ are the sub-matrices of the hydrodynamic and static forces, and $\vec{x}\left(P^N\right)$ and $\vec{x}\left(P^0\right)$ are the coordinates of the anchor and fairlead nodes.

2.4. Lumped-mass mooring dynamics model

In this study, the lumped-mass mooring model MoorDyn [16] is coupled with the numerical framework REEF3D. The mooring line is discretized into N equally distanced bars with N+1 nodes. The first and last nodes, $\mathbf{r}_0$ and $\mathbf{r}_N$, are connected to the bottom (anchor node) and the floating body (fairlead node). The line segment between two consecutive nodes has an index of 1/2. Each node is represented by a global vector $\mathbf{r} = \mathbf{r}(x, y, z)$, defined in the inertial reference system. This method includes internal damping, seabed interaction, and hydrodynamic forces acting on the nodes are calculated by using Morison's formula as drag and added mass forces. The complete equation of motion for each node i is obtained as in Eq. (20). Here, $\mathbf{m}_i$ is a 3 x 3 mass matrix, $\mathbf{a}_i$ is the added mass forces, $\mathbf{T}$ is the tension force in the segments, $\mathbf{C}$ is the internal damping force, $\mathbf{W}_i$ is the submerged weight, $\mathbf{B}_i$ is the vertical force due to the mooring line seabed interaction, and $\mathbf{D}_{pi}$ and $\mathbf{D}_{qi}$ are the hydrodynamic forces transverse and tangential directions.

$$[\mathbf{m}_i + \mathbf{a}_i]\,\ddot{r}_i = \mathbf{T}_{i+1/2} - \mathbf{T}_{i-1/2} + \mathbf{C}_{i+1/2} - \mathbf{C}_{i-1/2} + \mathbf{W}_i + \mathbf{B}_i + \mathbf{D}_{pi} + \mathbf{D}_{qi} \tag{20}$$

The system of equations above is solved for all nodes of the mooring line with a constant-time-step second-order Runge-Kutta (RK2) integration algorithm.

3. RESULTS

The upgraded rigid-body FSI algorithm is tested with a full-scale semisubmersible structure OC5. The experimental results are taken from the OC5-DeepCwind floating semisubmersible offshore wind test campaign, which was carried out at MARIN's offshore wave basin

[31]. The structure's properties and mooring lines configuration are obtained from [31]. The OC5 system properties are outlined in Table 2. For the numerical analysis, a numerical wave tank (NWT) is created with dimensions of 1500 m in length, 210 m in width, and 250 m in height, and a constant water depth of 200 m. The FOWT is placed at the center of the NWT. The semi-submersible structure is simulated under two different regular wave conditions, as specified in Table 1. A 2nd-order Stokes theory is used to generate waves along with the relaxation method which is employed for both wave generation and absorption.

Table 1: Wave Conditions [31]

Sea state	**H (m)**	**T (s)**	**Steepness**
Regular wave - 1	7.37	12.07	0.0324
Regular wave - 2	9.41	14.3	0.0295

The platform motions are restrained with three mooring lines in waves as depicted in Fig. 2 (a). Detailed information about the mooring system can be found in [31]. A native quasi-static mooring model is available in the numerical framework. Additionally, the lumped-mass mooring model MoorDyn [16] is coupled with the numerical framework REEF3D. The mooring lines are divided into 40 elements and the same settings and parameters (mooring line diameter, mooring line mass per unit length, mooring line length, and mooring axial stiffness) are used for both mooring models. The mooring tensions are calculated by these two models and the results are presented.

Table 2: OC5 System structural proporties [31]

Mass	1.3958E+7 kg
Draft	20 m
Displacement	1.3917E+4 m^3
CM location below SWL	8.07 m
Roll inertia about system CM	1.3947E+10 $kg.m^2$
Pitch inertia about system CM	1.5552E+10 $kg.m^2$
Yaw inertia about system CM	1.3692E+10 $kg.m^2$

The grid stretching applied around the semisubmersible and the free surface is depicted in Fig. 2 (b). The maximum and minimum cell sizes for the grid convergence study are given in Table 3. The results of the grid convergence study are shown in Fig. 1. It is seen that the motion responses with the medium and fine grids are similar and the fine grid is selected for the simulations. The wind dynamics are not considered in the experiment.

Figs. 3 and 4 show the FOWT free-surface interaction with horizontal velocity contour. Fig. 5 presents the heave, pitch, and surge motions of the semisubmersible alongside the corresponding experimental results for wave- 1. In Fig. 5 (a), the heave motion in wave-1 shows a minor overestimation but good agreement in amplitude and phase with both mooring models. Pitch motion is depicted in Fig. 5 (b), matching the experimental data quite well for both mooring models. Fig. 5 (c) depicts surge motion results over time,

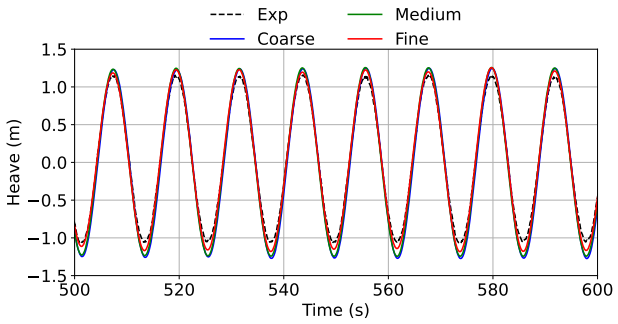

(a) Heave motion

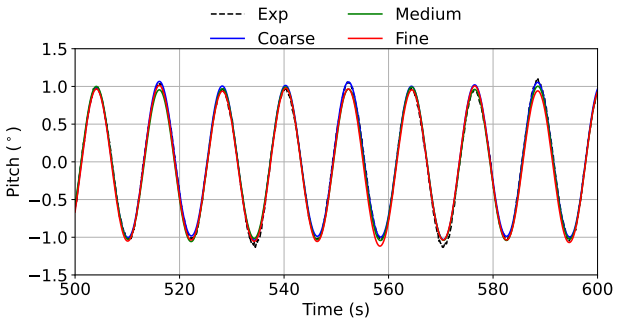

(b) Pitch motion

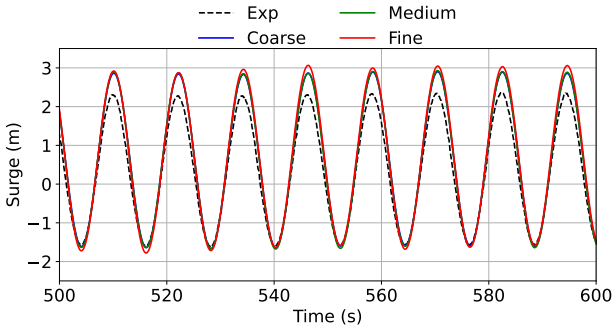

(c) Surge motion

Figure 1: Grid convergence study for the motion responses in wave-1.

showing overestimations in the peaks, yet demonstrating good agreement in the troughs. The numerical results obtained with two different mooring models are quite similar in general.

Fig. 6 presents the motion responses of the platform in wave - 2. Fig. 6 (a) shows the heave motion results. The numerical results match well with the experimental data, yet the peaks of the amplitude are slightly underestimated with both mooring models. The peaks of the pitch motion, on the other hand, match with the experimental results as depicted in 6 (b). However, the troughs tend to be underestimated for both mooring models. Fig. 6 (c) shows the time series of surge motion results, demonstrating good agreement even though there are some slightly over- and underestimations for peaks and troughs.

Fig. 7 presents the fairlead tensions calculated by the quasi-static mooring model and

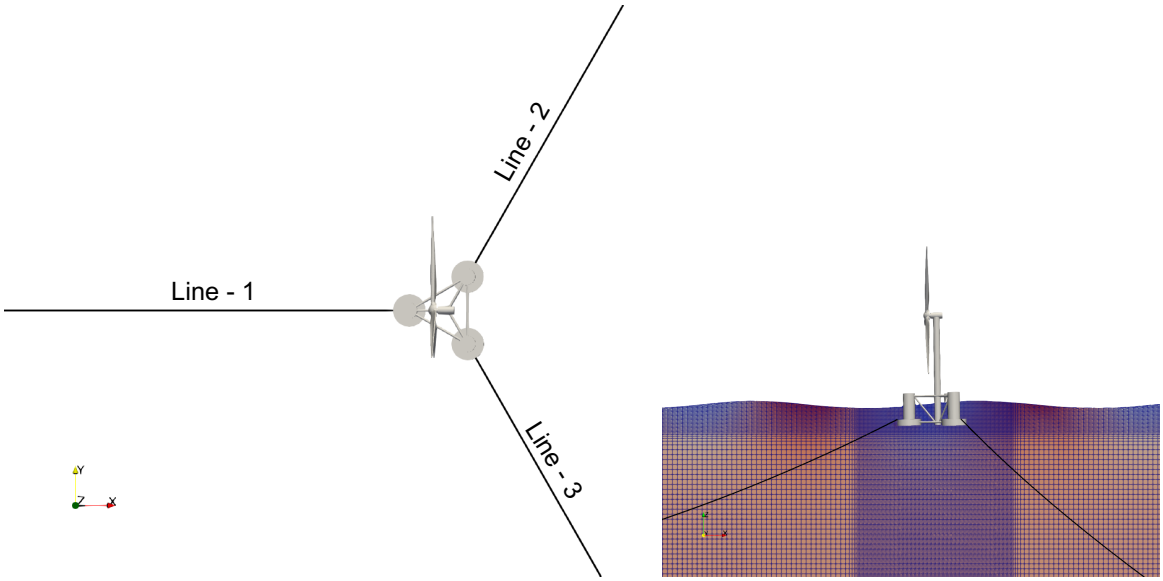

(a) Mooring Lines and Structre

(b) Grid Stretching around the body and the free-surface

Figure 2: OC5 Platform

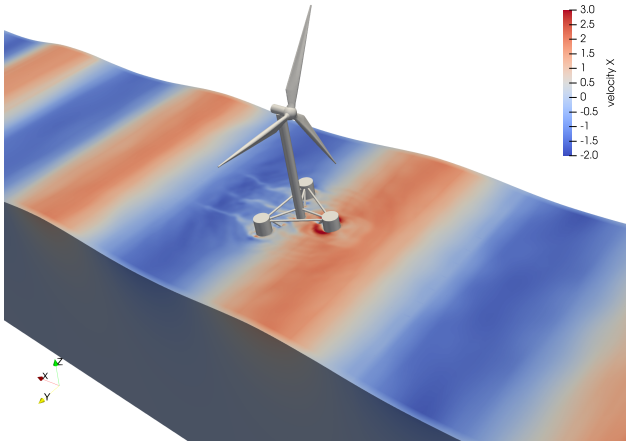

Figure 3: The FOWT free-surface interaction in wave - 1, showing the horizontal velocity contour, perspective view

MoorDyn in wave - 1. The results show a slight phase shifting between the mooring models and the magnitude of the fairlead tensions are different, even though the order of magnitude of the fairlead tensions is similar. Fig. 8 illustrates the corresponding power spectral density (PSD) of the fairlead tensions in wave - 1. The large peaks can be seen at 0.0828 Hz which is consistent with the corresponding wave frequency. The results indicate that MoorDyn predicts a larger excitation than the quasi-static mooring model.

Fairlead tensions and the corresponding power spectral density (PSD) in wave -2 are given in Fig. 9 and Fig. 10, respectively. The same outcomes with wave - 1 condition can

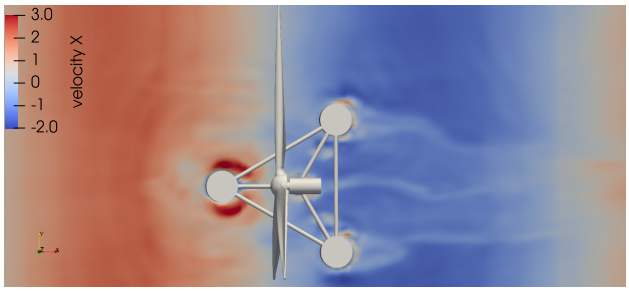

(a) Wave-1

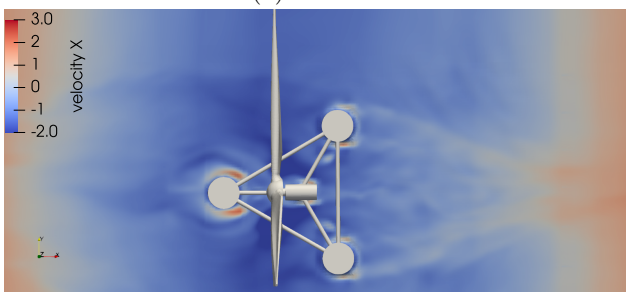

(b) Wave-2

Figure 4: The FOWT free-surface interaction, showing the horizontal velocity contour, top view

Table 3: Grid convergence study for the motion responses

Grid	Δx_{min} Δy_{min} Δz_{min} [m]	Δx_{max} Δy_{max} Δz_{max} [m]	Stretching Ratio [-]	Number of cells [-]
Coarse	1.56	7.8	0.1	1,939,520
Medium	1.2	6.0		3,435,978
Fine	1.0	5.0		5,697,606

be observed in wave -2. Based on the results presented in this study, it can be concluded that in such regular wave conditions, the mooring line algorithm has a minor effect on the motion response of the platform. Additionally, the outcomes from this study are consistent with the results in [16, 32].

While the most deviation for the motion responses is seen in the surge motion in wave-1 (Fig. 5 (c)), it is also seen in the pitch motion in wave-2 (Fig. 6 (b)). Given that the mooring model exerts a negligible influence on the motion responses, this deviation could be linked to the possible uncertainties in representing the parameters of the center of gravity, center of rotation, and moment of inertia within the numerical model. Slight variations in these parameters could result in deviations from the anticipated values.

The dynamic mooring model, as presented in this study, was specifically designed to capture snap load conditions. However, snap load conditions could not be observed in this study. Nevertheless, tensions obtained by the quasi-static mooring model are lower

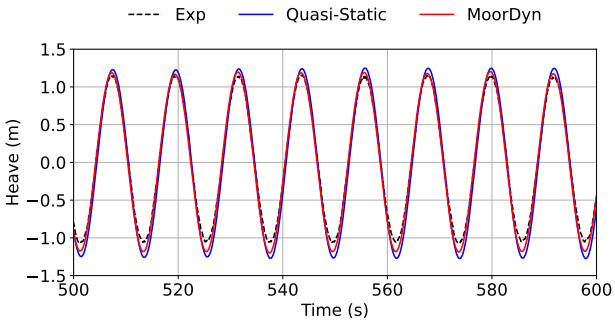

(a) Heave motion

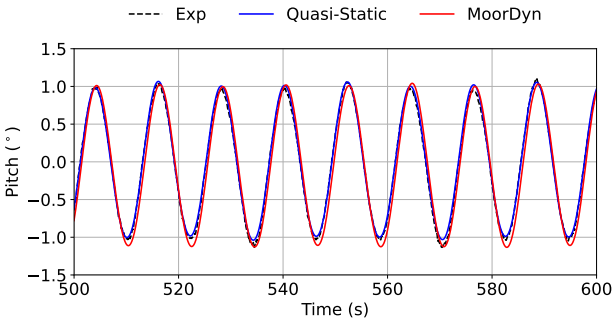

(b) Pitch motion

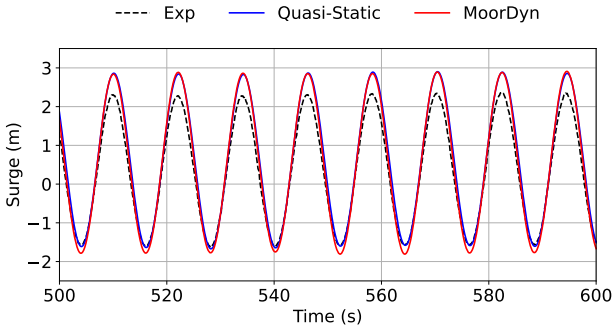

(c) Surge motion

Figure 5: Comparison of the motion response amplitude time history and experimental results for wave-1.

than the tension results of the dynamic mooring model. This difference may arise from neglecting the mooring dynamics effects in the quasi-static mooring model. On the other hand, tension results obtained by the dynamic mooring model exhibit nonlinearity, while the quasi-static mooring model produces predominantly linear results, as expected. It is also worth mentioning that the quasi-static mooring model captures all dominant frequency components, even though the magnitudes of the results are lower.

4. CONCLUSION

In this study, the upgraded direct forcing immersed boundary method is tested with a native quasi-static mooring model and the lumped-mass mooring model MoorDyn. The

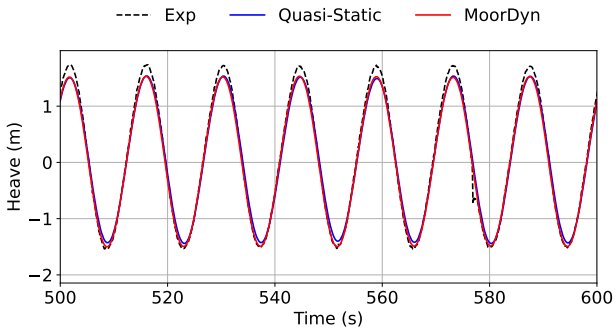

(a) Heave motion

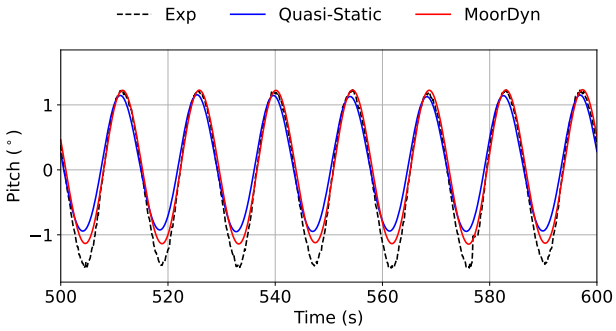

(b) Surge motion

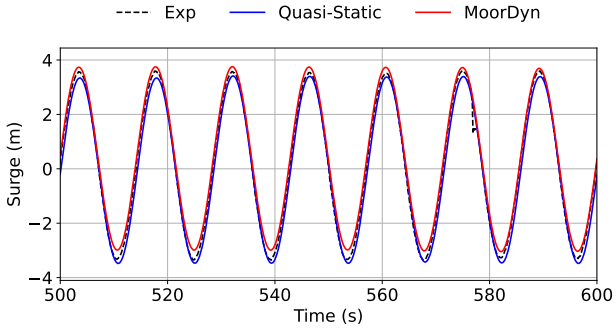

(c) Surge motion

Figure 6: Comparison of the motion response amplitude time history and experimental results for wave - 2.

motion responses of the semisubmersible platform demonstrated generally good agreement with experimental results, with minor discrepancies.

While both mooring models rely on similar numerical approaches and assumptions, the primary distinction lies in the simplification inherent to the quasi-static mooring model. This model assumes steady-state flow and small line motion in time. The fairlead tensions calculated by the two mooring models show some phase shifting, and MoorDyn predicted larger excitation compared to the quasi-static mooring model. This may be attributed to the simplification made for the quasi-static mooring model. Nevertheless, the quasi-static mooring model can capture all dominant frequency components, which is crucial for mooring design in coastal engineering applications.

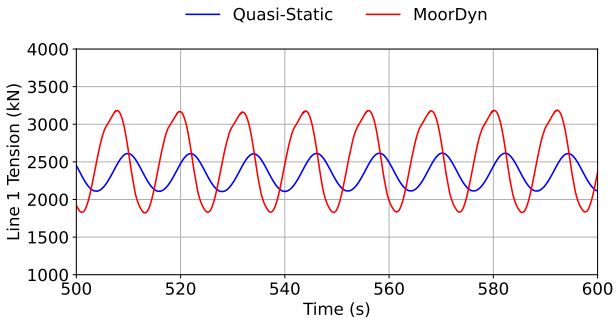

(a) Mooring Line-1

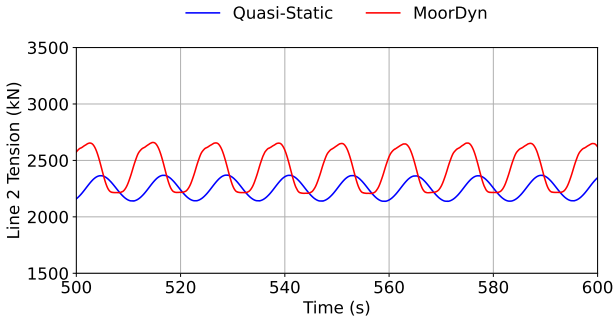

(b) Mooring Line-2

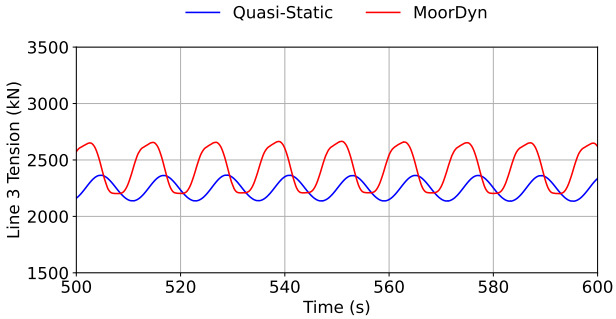

(c) Mooring Line-3

Figure 7: Comparison of fairlead tensions in wave - 1.

Given the results presented in this study, the choice of the mooring line algorithm has a minor impact on the motion response of the platform in regular wave conditions, and the motion responses can be safely calculated with the quasi-static mooring model in such conditions. However, the results also indicate that the dynamic mooring model is needed for a reliable mooring line force and fatigue analysis. Furthermore, the findings in this study align with the outcomes reported in the existing literature.

In summary, this study shows that the enhanced direct forcing immersed boundary method integrated quasi-static mooring algorithm in REEF3D::CFD is capable of simulating the motions and mooring line responses of the submersible structures in waves.

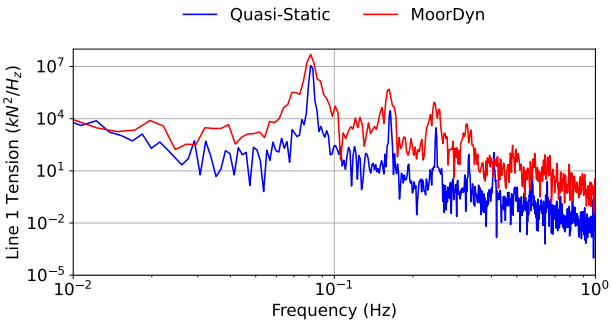

(a) Mooring Line-1

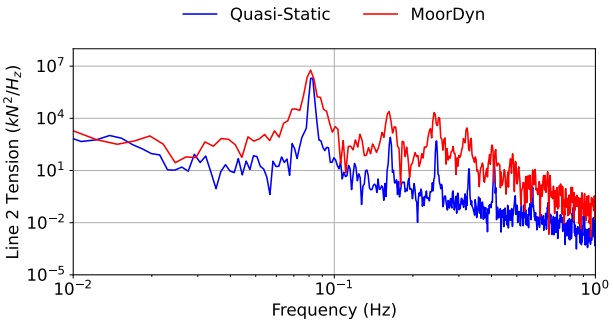

(b) Mooring Line-2

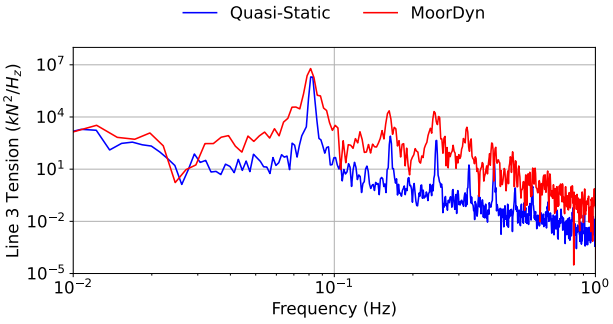

(c) Mooring Line-3

Figure 8: Comparison of fairlead tensions PSDs in wave - 1.

Acknowledgments

This work was made possible through the knowledge-building project Improving Performance in Real Sea, IPIRiS, financially supported by the Norwegian Research Council, NFR project number 308843, and the consortium partners.

References

[1] S. Burmester, G. Vaz, O. el Moctar, Towards credible CFD simulations for floating offshore wind turbines, Ocean Engineering 209 (2020) 107237.

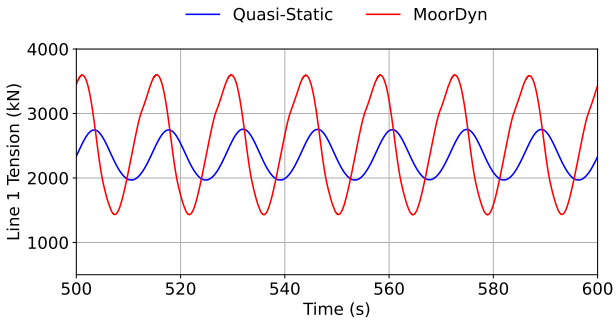

(a) Mooring Line-1

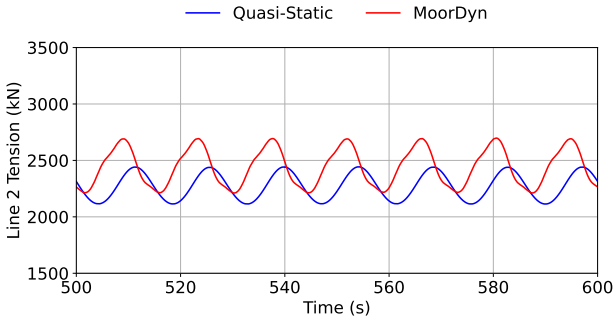

(b) Mooring Line-2

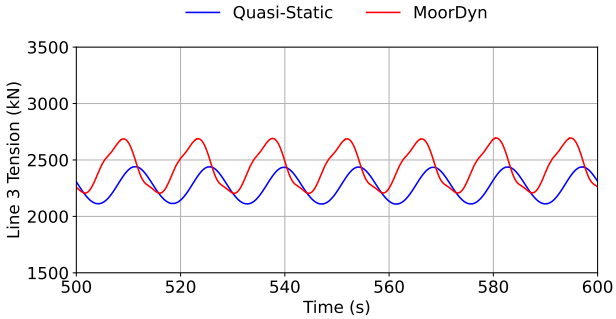

(c) Mooring Line-3

Figure 9: Comparison of fairlead tensions in wave - 2.

[2] G. Vaz, F. Jaouen, M. Hoekstra, Free-surface viscous flow computations: Validation of URANS code FRESCO, in: International Conference on Offshore Mechanics and Arctic Engineering, vol. 43451, 425–437, 2009.

[3] Y. Wang, H.-C. Chen, A. Koop, G. Vaz, Verification and validation of CFD simulations for semi-submersible floating offshore wind turbine under pitch free-decay motion, Ocean Engineering 242 (2021) 109993.

[4] Y. Wang, H.-C. Chen, A. Koop, G. Vaz, Hydrodynamic response of a FOWT semi-submersible under regular waves using CFD: Verification and validation, Ocean Engineering 258 (2022) 111742.

[5] H. Huang, H.-C. Chen, Investigation of mooring damping effects on vortex-induced motion of a deep draft semi-submersible by coupled CFD-FEM analysis, Ocean Engineering 210 (2020) 107418.

[6] P. Cheng, Y. Huang, D. Wan, A numerical model for fully coupled aero-hydrodynamic analysis of floating offshore wind turbine, Ocean Engineering 173 (2019) 183–196.

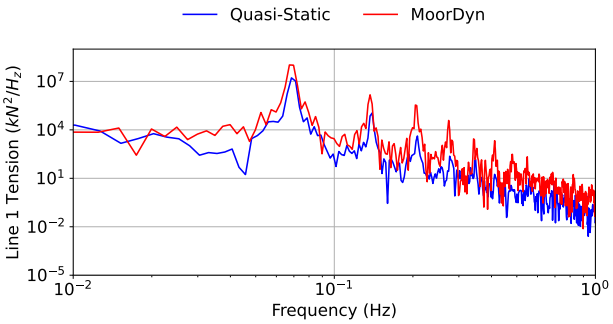

(a) Mooring Line-1

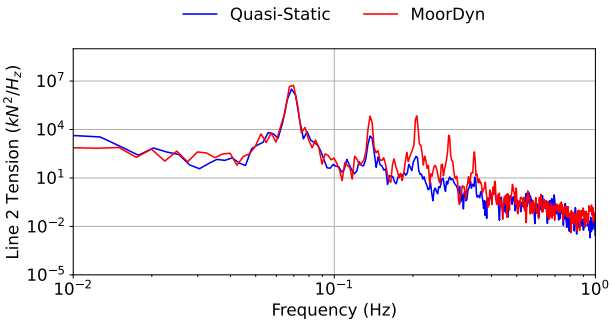

(b) Mooring Line-2

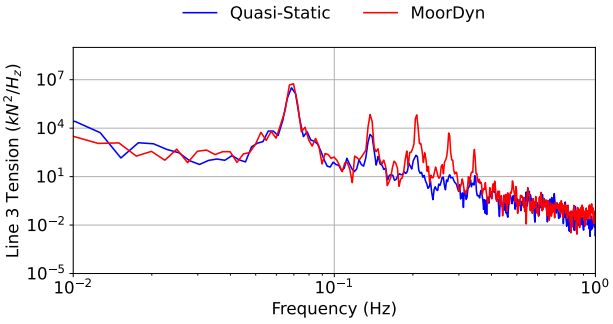

(c) Mooring Line-3

Figure 10: Comparison of fairlead tensions PSDs in wave - 2.

[7] P. Li, P. Cheng, D. Wan, Q. Xiao, Numerical simulations of wake flows of floating offshore wind turbines by unsteady actuator line model, in: Proceedings of the 9th international workshop on ship and marine hydrodynamics, Glasgow, UK, 26–28, 2015.

[8] Y. Liu, Q. Xiao, A. Incecik, C. Peyrard, D. Wan, Establishing a fully coupled CFD analysis tool for floating offshore wind turbines, Renewable Energy 112 (2017) 280–301.

[9] T. T. Tran, D.-H. Kim, Fully coupled aero-hydrodynamic analysis of a semi-submersible FOWT using a dynamic fluid body interaction approach, Renewable energy 92 (2016) 244–261.

[10] T. T. Tran, D.-H. Kim, A CFD study of coupled aerodynamic-hydrodynamic loads on a semisubmersible floating offshore wind turbine, Wind Energy 21 (1) (2018) 70–85.

[11] H. Bihs, A. Kamath, M. A. Chella, A. Aggarwal, Ø. A. Arntsen, A new level set numerical wave tank with improved density interpolation for complex wave hydrodynamics, Computers & Fluids 140 (2016) 191–208.

[12] T. Martin, G. Wang, H. Bihs, Numerical Modelling of the Interaction of Moving Fish Nets and Fluid Volume 5: Ocean Space Utilization (2020) V005T05A004, URL https://doi.org/10.1115/OMAE2020-18605.
[13] T. Martin, H. Bihs, A CFD Approach for Modelling the Fluid-Structure Interaction of Offshore Aquaculture Cages and Waves Volume 6: Ocean Engineering (2021) V006T06A041, doi:10.1115/OMAE2021-61808, URL https://doi.org/10.1115/OMAE2021-61808.
[14] T. Martin, A. Kamath, H. Bihs, Accurate modeling of the interaction of constrained floating structures and complex free surfaces using a new quasistatic mooring model, International Journal for Numerical Methods in Fluids 93 (2) (2021) 504–526.
[15] G. Wang, T. Martin, L. Huang, H. Bihs, Numerical investigation of the hydrodynamics of a submersible steel-frame offshore fish farm in regular waves using CFD, Ocean Engineering 256 (2022) 111528, ISSN 0029-8018, doi:https://doi.org/10.1016/j.oceaneng.2022.111528, URL https://www.sciencedirect.com/science/article/pii/S0029801822008952.
[16] M. Hall, A. Goupee, Validation of a lumped-mass mooring line model with DeepCwind semisubmersible model test data, Ocean Engineering 104 (2015) 590–603.
[17] A. Soydan, W. Wang, H. Bihs, An Improved Direct Forcing Immersed Boundary Method for Simulating Floating Objects, 10th Conference on Computational Methods in Marine Engineering doi: 10.23967/marine.2023.035.
[18] S. Osher, J. A. Sethian, Fronts Propagating with Curvature-Dependent Speed: Algorithms Based on Hamilton-Jacobi Formulations, Journal of Computational Physics 79 (1988) 12–49.
[19] M. Sussman, P. Smereka, S. Osher, A Level Set Approach for Computing Solutions to Incompressible Two-Phase Flow, Journal of Computational Physics 114 (1994) 146–159.
[20] D. Peng, B. Merriman, S. Osher, H. Zhao, M. Kang, A PDE-based fast local level set method, Journal of Computational Physics 155 (1999) 410–438.
[21] G.-S. Jiang, C.-W. Shu, Efficient implementation of weighted ENO schemes, Journal of computational physics 126 (1) (1996) 202–228.
[22] G. Jiang, D. Peng, Weighted ENO schemes for Hamilton Jacobi equations, SIAM Journal of Scientific Computing Volume 21 (2000) 2126–2143.
[23] L. J. Timmermans, P. D. Minev, F. N. Van De Vosse, An approximate projection scheme for incompressible flow using spectral elements, International journal for numerical methods in fluids 22 (7) (1996) 673–688.
[24] T. Martin, T. A., H. Bihs, numerical framework for modelling the dynamics of open ocean aquaculture structures in viscous fluids, Applied Ocean Research 106 (2021) 102410.
[25] C. Shu, S. Osher, Efficient implementation of essentially non-oscillatory shock-capturing schemes, Journal of Computational Physics Volume 77(2) (1988) 439–471.
[26] H. van der Vorst, BiCGStab: A fast and smoothly converging variant of Bi-CG for the solution of nonsymmetric linear systems, SIAM Journal of Scientific Computing Volume 13 (1992) 631–644.
[27] S. Ashby, R. Flagout, A parallel mulitgrid preconditioned conjugate gradient algorithm for groundwater flow simulations, Nuclear Science and Engineering Volume 124(1) (1996) 145–159.
[28] L. Yang, One-fluid formulation for fluid–structure interaction with free surface, Computer Methods in Applied Mechanics and Engineering 332 (2018) 102–135, ISSN 0045-7825, doi: https://doi.org/10.1016/j.cma.2017.12.016.
[29] H. Bihs, A. Kamath, M. Alagan Chella, C. Pakozdi, Complex geometry handling for a cartesian grid based solver, in: MekIT'17-Ninth national conference on Computational Mechanics, International Center for Numerical Methods in Engineering (CIMNE), 2017.
[30] J. Palm, C. Eskilsson, L. Bergdahl, An hp-adaptive discontinuous Galerkin method for modelling snap loads in mooring cables, Ocean Engineering 144 (2017) 266–276.
[31] A. N. Robertson, F. Wendt, J. M. Jonkman, W. Popko, H. Dagher, S. Gueydon, J. Qvist, F. Vittori, J. Azcona, E. Uzunoglu, et al., OC5 project phase II: validation of global loads of the DeepCwind floating semisubmersible wind turbine, Energy Procedia 137 (2017) 38–57.
[32] H. Chen, M. Hall, CFD simulation of floating body motion with mooring dynamics: Coupling MoorDyn

with OpenFOAM, Applied Ocean Research 124 (2022) 103210.